Available online at www.sciencedirect.com
ScienceDirect
Journal of the European Ceramic Society 31 (2011) 2309–2317
www.elsevier.com/locate/jeurceramsoc

Structural, microstructural and electrical properties evolution of (K,Na,Li)(Nb,Ta,Sb)O_3 lead-free piezoceramics through NiO doping

F. Rubio-Marcos [a,*], P. Marchet [a], J.J. Romero [b], J.F. Fernández [b]

[a] *Laboratoire de Science des Procédés Céramiques et de Traitements de Surface, UMR 6638 CNRS, Université de Limoges, Centre Européen de la Céramique, 12, rue Atlantis, 87068, Limoges Cedex, France*

[b] *Electroceramic Department, Instituto de Cerámica y Vidrio, CSIC, Kelsen 5, 28049, Madrid, Spain*

Received 12 April 2011; received in revised form 23 May 2011; accepted 27 May 2011
Available online 21 June 2011

Abstract

Excellent piezoelectric properties have been reported in the (K,Na)NbO_3–$LiTaO_3$–$LiSbO_3$ system and have been regarded as a new candidate of lead-free piezoelectric material. Nevertheless, there are still some structural and electrical aspects that remain controversial with respect to the role of dopants in this system. NiO doping modifies the (K,Na,Li)(Nb,Ta,Sb)O_3 structure, giving rise to the appearance of the TTB-like secondary phase and to changes on the orthorhombic to tetragonal phase transition temperature. The microstructural characterization reveals that sintering process is assisted by a transient liquid phase. The presence of Ni in the liquid phase indicates that Ni^{II} ions could act as new nucleus for the secondary phase crystallization. Thus, as higher the amounts of liquid phase, higher the secondary phase appearance. The modifications on the structure and microstructure of the system cause a reduction of the piezoelectric constant, which is accompanied by an increase on the mechanical quality factor.

Keywords: A. Powders-solid state reaction; B. Microstructure-final; C. Piezoelectric properties; D. Niobates

1. Introduction

Currently, lead zirconate titanate (PZT) family ceramics are widely used as piezoelectric materials, due to their high piezoelectric response. Lead is a very toxic element and is now being progressively removed from industrial processes. The European Union has published a health normative (ROH)[1] avoiding the use of lead because of its toxicity and environmental risks. Nevertheless, PZT ceramics are still allowed because of the lack of an adequate alternative. Among the available lead-free ferroelectric ceramics, one promising candidate is the family of sodium potassium niobate (K,Na)NbO_3 (KNN), on account of its good electromechanical properties.[2] As for PZT, the sinterability of KNN-based materials can be improved by using different sintering aids and dopants, such as CuO,[3,4] SnO_2,[5] ZnO[6] and MnO.[7] These chemical elements usually enter in B position of the ABO_3 perovskite structure and thus produce A-site vacancies that suppress the formation of the hygroscopic secondary products responsible from the deliquescence problems of KNN.[8] Some studies have also been carried out concerning the formation of solid solutions, such as KNN–$BaTiO_3$,[9] KNN–$LiNbO_3$,[10] KNN–$LiTaO_3$,[11–13] KNN–$LiSbO_3$.[14]

Excellent piezoelectric properties have been reported in the (K,Na)NbO_3–$LiTaO_3$–$LiSbO_3$ system prepared by a complex processing method.[15] These results have opened up a challenge to obtain lead free piezoceramics with good properties through different routes, especially those correlated with a technological and economically available process. At the present time, these compounds can be seriously considered as candidates for the substitution of PZT. Nevertheless, some of their properties are not suitable for all purpose.

Recently, we have reported in the (K,Na,Li)(Nb,Ta,Sb)O_3 system (abbreviated as KNL–NTS), that the dielectric, piezoelectric and elastic material responses are fundamentally related to extrinsic effects.[16] Nonetheless, the dielectric and mechanical losses at room temperature are similar to those of a soft PZT ceramic and too high to be used in power devices. Thus, they need to be modified by the use of suitable dopants, like for "pure" KNN. The effect of doping on various physical and chemical properties of this material is known. Many

* Corresponding author. Tel.: +33 5 87 50 23 77; fax: +33 5 87 50 23 07.
E-mail address: fernando.rubio-marcos@unilim.fr (F. Rubio-Marcos).

0955-2219/$ – see front matter © 2011 Elsevier Ltd. All rights reserved.
doi:10.1016/j.jeurceramsoc.2011.05.041

aliovalent compositional modifications to KNN-based system have been studied either with higher valence substitutions (donors), or with lower valence ions (acceptors). In the present work, NiO was selected as the dopant of KNL–NTS ceramics. Thus, on the basis of ionic radii,[17] the Ni^{II} ion ($r_{Ni}{}^{2+}$: 0.69 Å for a coordination number CN = 6) could substitute in either A or B-sites. Considering its valency, Ni^{II} can either act as donor-dopant if introduced in A-site or as an acceptor-dopant in B-site. Such behaviors may cause several effects on the dielectric behavior through interaction with structure perovskite.

In order to study the doping effect of Ni^{II} ion into KNN-based perovskite lattice, we selected A-site deficiency formulation $(K_{0.44}Na_{0.52}Li_{0.04})_{(1-x)}Ni_{(x/2)}(Nb_{0.86}Ta_{0.10}Sb_{0.04})O_3$ by two reasons; (i) in this case, and as previously reported[18,19] A-site deficiency (and thus excess B^{+5} cations) improved the sinterability and (ii) for this A-deficient composition, the densification occurs via a liquid phase that promotes grain growth and improves sintering, but induces the occurrence of a secondary phase of tetragonal tungsten bronze (TTB) structure, similar to the one observed for $LiTaO_3$[12] and $LiNbO_3$ modified KNN.[20]

This paper will present and discuss the effects of such NiO substitution on the structure, microstructure, dielectric and piezoelectric properties of $(K_{0.44}Na_{0.52}Li_{0.04})_{1-x}Ni_{x/2}](Nb_{0.86}Ta_{0.10}Sb_{0.04})O_3$ ceramics.

2. Experimental details

2.1. Preparation of $(KNL)_{1-x}Ni_{x/2}$–NTS ceramics

The $[(K_{0.44}Na_{0.52}Li_{0.04})_{1-x}Ni_{x/2}]$ $(Nb_{0.86}Ta_{0.10}Sb_{0.04})O_3$ compositions with $x = 0.000$, 0.005, 0.010, 0.030 and 0.050, hereafter abbreviated as $(KNL)_{1-x}Ni_{x/2}$–NTS, were synthesized by conventional solid-state reaction.[21] The raw materials used in this study are potassium carbonate (K_2CO_3, 99.0%), sodium carbonate (Na_2CO_3, 99.5%), lithium carbonate (Li_2CO_3, 99.5%), nano-nickel oxide (NiO, 99.9%), niobium oxide (Nb_2O_5, 99.5%), tantalum oxide (Ta_2O_5, 99.0%) and antimony oxide (Sb_2O_5, 99.995%). NiO nano-powders (mean primary particle diameter ~15 nm) were selected because they could improve the sinterability and lead to better compositional homogenization.

Because of their hygroscopic nature, the raw materials were dried at 200 °C for 1 h before all the experiments. They were also milled individually, in order to obtain an appropriate particle size distribution. This step is crucial to improve the homogeneity of the mixture of the reacting materials and therefore to control the compositional homogeneity of both the calcined powders and the sintered ceramics.[22] These powders were then weighed and mixed by attrition-milling using ZrO_2 balls in absolute ethanol medium for 3 h, dried and calcined at 700 °C for 2 h. The calcined powders were attrition milled again and cold-isostatically pressed at 200 MPa into disks of 10 mm in diameter and 0.7 mm in thickness. The pellets were finally sintered in air at 1125 °C for 16 h.

2.2. Structural characterization

The crystalline structure was studied by X-ray diffraction (XRD, Siemens D5000, Cu Kα radiation) on powder obtained by milling of the sintered ceramics. The lattice parameters were refined by a global simulation of the full diagram (pattern matching, *fullprof* program). Raman spectra were measured in air atmosphere at room temperature, using the 514 nm radiation from an Ar^+ laser operating at 10 mW. The signal was collected by a microscope Raman spectrometer (Renishaw Micro-Raman System 1000) in the 100–1100 cm^{-1} range.

2.3. Microstructural characterization

Microstructure was evaluated on polished and thermally etched samples (1000 °C for 5 min) using a field emission scanning electron microscope, FE-SEM (Hitachi S-4700, Tokio, Japan), fitted out with energy dispersive spectroscopy, EDS. The average grain size was determined from FE-SEM micrographs by an image processing and analysis program (Leica Qwin, Leica Microsystems Ltd., Cambridge, England) considering more than 500 grains in each measurement.

2.4. Electrical characterization

Electrical characterization was carried out on ceramic discs with fired silver paste (700 °C) on both sides as electrodes. The temperature dependence of the ceramics permittivity was measured using an impedance analyzer (HP4294A, Agilent) in the frequency range of 100 Hz–1 MHz and the temperature range of 30–600 °C, using a 2 °C/min heating rate.

Piezoelectric properties were evaluated, after a classical poling process. This process was carried out in a silicone oil bath at 25 °C under a DC electric field of 40 kV/cm during 30 min. The piezoelectric constant d_{33} was measured using a piezo-d_{33} meter (YE2730A d_{33} METER, APC International). The piezoelectric constant d_{31} was determined at room temperature by the resonance/antiresonance method on the basis of IEEE standards. The planar mechanical quality, Q_m, which is related to the sharpness of the resonance frequency, was calculated using the following equation described in ref. 23:

$$Q_m = \frac{f_a^2}{2\pi f_r Z_m C^T (f_a^2 - f_r^2)} \quad (1)$$

where f_r is the resonance frequency (Hz), f_a is the antiresonance frequency (Hz), Z_m is the minimum impedance at f_r (ohm) resonance impedance, C^T is the capacitance mechanically free at 1 kHz.

Finally, the ferroelectric nature of the ceramics was determined using a hysteresis meter (RT 6000 HVS, RADIANT Technologies) operating in virtual ground mode.

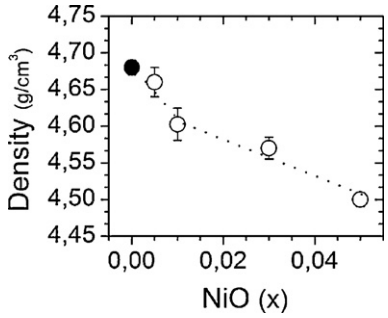

Fig. 1. Density of the $(KNL)_{1-x}Ni_{x/2}$–NTS as a function of the NiO content for the ceramics sintered at 1125 °C during 16 h.

3. Results

3.1. Structural characterization

Fig. 1 shows the bulk densities of the $(KNL)_{1-x}Ni_{x/2}$–NTS ceramics as function of the NiO content. As the NiO addition increases, the bulk density decreases and reaches minimum value of 4.50 ± 0.01 g/cm^3 for the ceramics with $x = 0.05$ of NiO.

The X-ray diffraction patterns of ceramics samples with different NiO amounts are displayed in Fig. 2(a). The patterns of all the ceramics show the diffraction peaks corresponding to perovskite-phase and a minor secondary-phase, which was assigned to $K_3LiNb_6O_{17}$[24] (KLN) or $K_6Nb_{10.88}O_{30}$ (PDF #87-1856), both with TTB type structure. Whatever the NiO amount, this secondary phase is always present.

Fig. 2(b) shows a magnification of the 2θ range running from 23.5° to 29.0°, where the most intense diffraction peaks of the secondary phase, TTB, can be clearly evidenced. XRD data showed that the TTB content evolves towards higher amount with increasing NiO content. For Li and Ta-modified (K,Na)NbO_3 piezoceramics, its occurrence was attributed to the volatilization and segregation of the alkali elements during sintering.[20] As a consequence, the TTB phase probably occurs here because of the A-site deficiency introduced by our choice of composition. The decrease in bulk density observed, at high values of x ($x > 0.01$) may be attributed to the higher concentration of the TTB secondary phase, which possesses a lower theoretical density (~4.376 g/cm^3) than the perovskite phase (~4.68 g/cm^3).

Moreover, as represented in Fig. 2(b), the NiO doping produces changes on the perovskite structure. For undoped material ($x = 0.00$), the splitting into (2 0 0) and (0 0 2) suggests a tetragonal symmetry, whereas for higher NiO content ($x \geq 0.03$), three peaks would be needed in order to correctly fit the XRD data, then suggesting orthorhombic symmetry. In order to further analyze the effect of NiO doping on the crystalline structure, the lattice parameters were calculated. Fig. 2(c) shows the variation of the lattice parameters as a function of the NiO amount. The refinement of the lattice parameters was performed using a tetragonal unit-cell (space group *P4mm*) for compositions with $x < 0.03$, and an orthorhombic unit-cell (space group *P222*) for compositions with $x \geq 0.03$. The intermediate state around $x \sim 0.02$, shadowed in this figure corresponds to the transitional region. For low NiO contents (the tetragonal symmetry range), the lattice parameters remain unchanged, where the tetragonal symmetry of the perovskite structure seems to be conserved. For higher NiO content ($x \geq 0.03$, orthorhombic range), the lattice parameters "*a*" and "*b*" increase with NiO content, while "*c*" slightly decreases. Thus, the structural distortion, *c*/*a*, Fig. 2(d), decreases linearly. Consequently, with increasing NiO content, we observed both the appearance of the TTB secondary phase and the transformation of the perovskite structure from tetragonal to orthorhombic symmetry.

The $(KNL)_{1-x}Ni_{x/2}$–NTS system sintered at 1125 °C for 16 h have also been investigated by Raman spectroscopy and the resulting spectra are depicted in Fig. 3(a). Raman spectroscopy has been used here to evidence the nature of the crystalline symmetry of the different compositions as function of the NiO content. Indeed, the Raman spectroscopy is a very sensitive tool to study at a local scale the structural deformations of perovskites, which are induced both by the tilting of BO_6 octahedra and by the cationic displacements, as it was well known for the piezoelectrics PZT and PMN–PT perovskite systems.[25,26] These structural modifications induce large changes in internal modes associated with BO_6 octahedron and thus a modification of the Raman spectra. The main vibrations observed here are associated to the BO_6 perovskite-octahedron[27,28] and consist of $1A_{1g}(\upsilon_1) + 1E_g(\upsilon_2) + 2F_{1u}(\upsilon_3,\ \upsilon_4) + F_{2g}(\upsilon_5) + F_{2u}(\upsilon_6)$ modes. Of these vibrations, $1A_{1g}(\upsilon_1) + 1E_g(\upsilon_2) + 1F_{1u}(\upsilon_3)$ are stretching modes and the other ones bending modes. In particular, $A_{1g}(\upsilon_1)$ and $F_{2g}(\upsilon_5)$ are detected as relatively strong scattering in systems similar to the one we are studying because of a near-perfect equilateral octahedral symmetry.

A detail of the region between 500 cm^{-1} and 700 cm^{-1} is presented in Fig. 3(b), for $(KNL)_{1-x}Ni_{x/2}$–NTS system. The insertion of Ni^{II} into the perovskite lattice slightly alters the observed vibrations frequencies as shown in Fig. 3(b). The $E_g(\upsilon_2)$ and $A_{1g}(\upsilon_1)$ peaks were fitted to the sum of two Lorentzian peaks. The peak $A_{1g}(\upsilon_1)$ shifts to lower wavenumber as NiO content increases (see Fig. 3(c)), due to a decrease in the strength constant force, caused by the lengthening of the distance between B^{5+} type ions and their coordinated oxygens.[29] As we noticed in a previous study,[30] the evolution of the $A_{1g}(\upsilon_1)$ Raman shift is similar to the evolution of the structural distortion parameter, *c*/*a*, observed by XRD: for low NiO content, there is no evolution of the Raman shift, while for $x > 0.01$, the Raman bands are substantially redshifted. This evolution suggests again that two different mechanisms are implied when NiO content is increased.

3.2. Microstructural characterization

The FE-SEM micrographs of the $(KNL)_{1-x}Ni_{x/2}$–NTS ceramics with x between 0.005 and 0.050 are shown in Fig. 4(a)–(d). The microstructure of undoped materials was previously reported[19,21] and consisted in homogeneously cubic-shaped grains with an average equivalent diameter of ~2 μm. The addition a low amount of the NiO produces an unhomogeneous grain growth; large grains of >20 μm are observed in competition with grain that resembled the undoped microstruc-

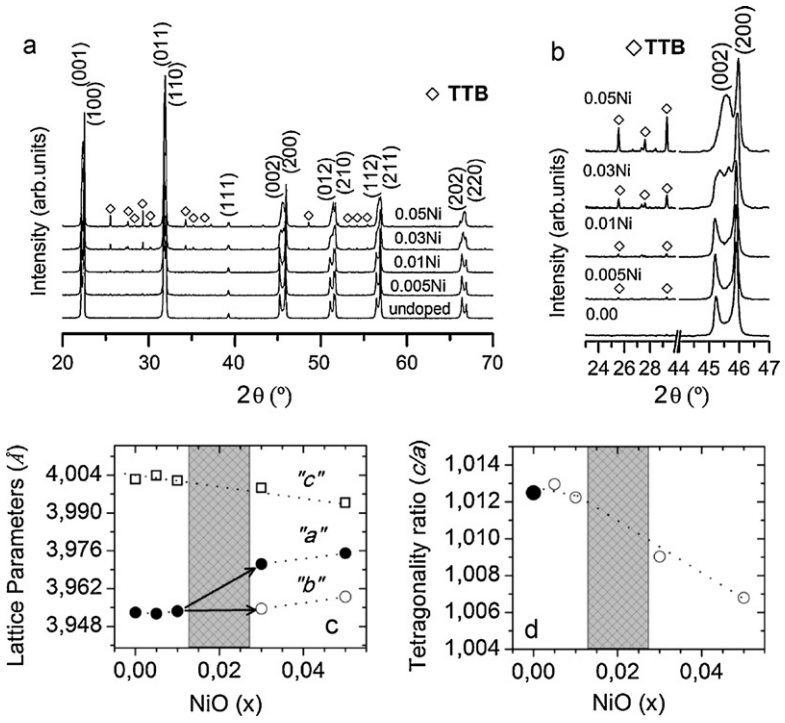

Fig. 2. (a) XRD patterns corresponding to the $(KNL)_{1-x}Ni_{x/2}$–NTS ceramics sintered at 1125 °C for 16 h. (b) Magnified XRD diffraction patterns in the 2θ range 23.5–29° and 44–47° of the $(KNL)_{1-x}Ni_{x/2}$–NTS ceramics (detail of the XRD on the region corresponding to (0 0 2) and (2 0 0) diffraction peaks). (c) Variation of lattice parameters of the $(KNL)_{1-x}Ni_{x/2}$–NTS ceramics as a function of the NiO content. (d) Variation of the tetragonality ratio, *c*/*a*, as a function of the NiO content.

ture (Fig. 4(a) and (b)). The appearance of secondary amorphous phase is associated with the transitory liquid phase that assisted sintering process (see inset Fig. 4(a)). This liquid phase has been also already observed in undoped samples only for short sintering time.[21] In this work, the liquid phase is stabilized for low NiO content. The presence of NiO enhanced probably the amount of transient liquid phase and thus the grain growth is promoted.

As the amount of NiO increase, the A-site deficiency increase and thus the liquid phase is promoted. However, higher amount of liquid phase produce the appearance of TTB phase that is distributed among the matrix grain. A change of the average grain size, as depicted in Fig. 4(a)–(d) with increasing NiO content is observed; the average grain size was homogenized and the microstructure shown average grain size > 5 μm, where a lower population of the large grains coexists.

As it has been discussed above, the liquid phase appears for the sample with lower NiO content. The occurrence of the transitory liquid phase is shown in detail Fig. 5(a) and the elemental composition of the liquid phase is pointed out by EDS (Fig. 5(b)). Table 1 lists the compositions measured by EDS on the liquid phase. When the quantity of the liquid phase is enlarged, secondary crystalline phases began to appear with a different morphology marked as point 2 in Fig. 5(b). This effect was more relevant for high NiO content. The EDS analysis reveals that the atomic percentages of elements change within the different grain regions. According with EDS analysis, the secondary

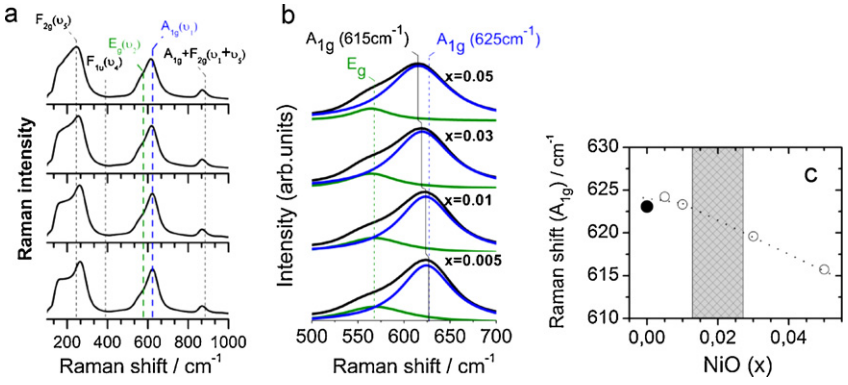

Fig. 3. (a) The Raman spectra of $(KNL)_{1-x}Ni_{x/2}$–NTS ceramics sintered at 1125 °C for 16 h. (b) Magnified Raman spectra in the range of the Raman shift from 440 to 760 cm^{-1} as function of the composition and Lorentzian fits of the individual peaks of the $E_g(\upsilon_2)$ and $A_{1g}(\upsilon_1)$ Raman modes. (c) Evolution of Raman shift of $A_{1g}(\upsilon_1)$ mode in function of the NiO content is also shown.

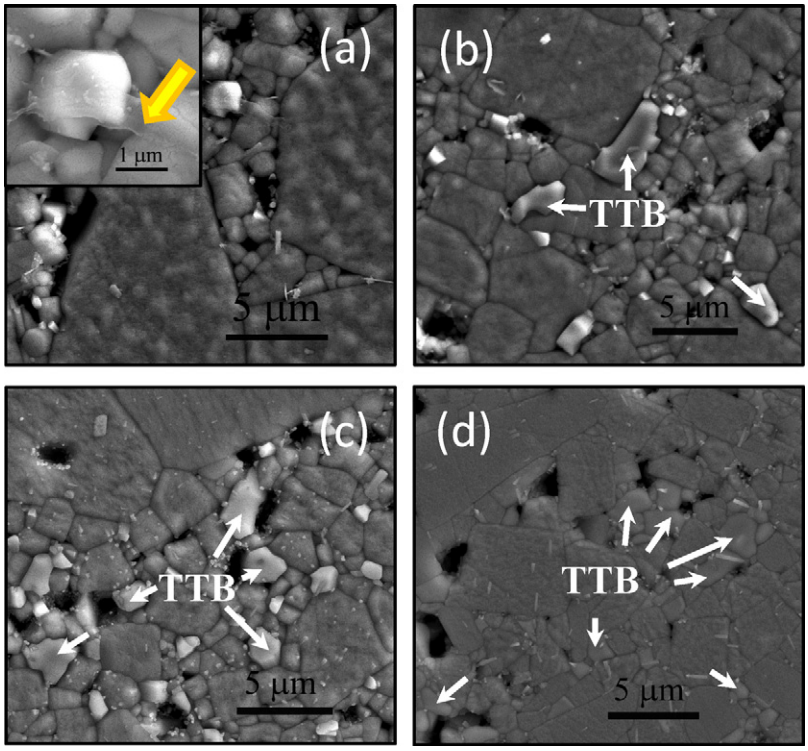

Fig. 4. Microstructure of polished and thermally etched surfaces of the $(KNL)_{1-x}Ni_{x/2}$–NTS ceramics sintered at 1125 °C for 16 h. (a) $x = 0.005$, (b) $x = 0.010$, (c) $x = 0.030$, and (d) $x = 0.050$. The inset of the Fig. 4(a) shows a detail of the liquid phase.

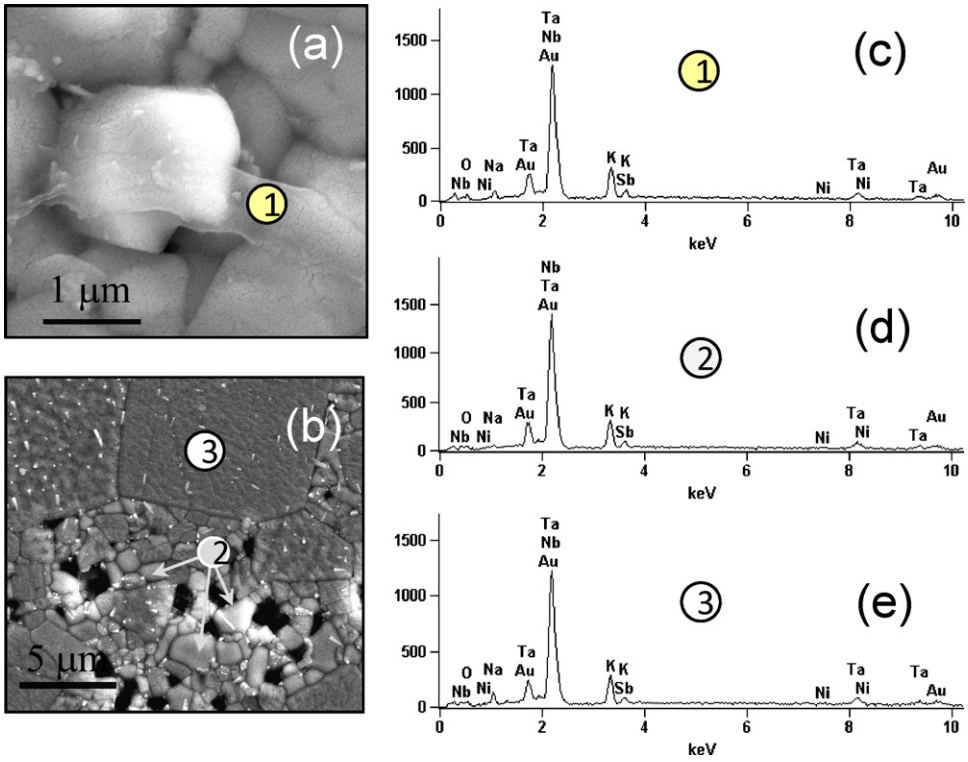

Fig. 5. Microphotographs of the $(KNL)_{1-x}Ni_{x/2}$–NTS ceramics with $x = 0.005$ (a) and $x = 0.050$ (b). Part (a) shows a detail of the liquid phase signalled with the point 1 while that the presence of a grain with TTB structure and a grain with nominal composition are signalled with the points 2 and 3 respectively, in part (b). EDS spectra of (c) the liquid phase (d) a TTB grain and (e) a matrix grain, corresponding to the ones marked as 1, 2 and 3, respectively, in Fig. 5(a) and (b).

Table 1
Composition on the points shown in Fig. 5 derived from EDS spectra. The table represents the atomic percentages of elements.

	O	Na	K	Li	Ni	Nb	Ta	Sb	Na/K
1. Liquid phase	62.56	6.22	8.67	–	0.13	19.31	2.04	1.07	0.72
2. TTB grain	64.27	2.17	9.70	–	0.16	20.33	2.30	1.07	0.22
3. Matrix grain	61.76	8.56	7.68	–	0.30	18.63	2.16	0.91	1.12
TTB[20] $Li_x(K_{0.78}Na_{0.22})_6(Nb_{0.86}Ta_{0.10}Sb_{0.04})_{10.9}O_{30}$	63.97	2.81	9.98	–	–	19. 99	2.32	0.92	0.28
KNL–NTS nominally composition	60.00	10.40	8.80	0.80	0.00	17.2	2.00	0.80	1.18

crystalline phase correspond to the TTB phase, observed by XRD, since the composition measured by EDS is quite similar to that of $Li_x(K_{0.78}Na_{0.22})_6(Nb_{0.86}Ta_{0.10}Sb_{0.04})_{10.9}O_{30}$ tungsten bronze material.[20] Although our results reveal that the TTB phase grains present a slight K^+-rich composition. This TTB based composition shows a low content of Ni^{II} (see Fig. 5(d)), indicating that the grains of TTB phase are formed to accommodate the NiO excess that cannot be incorporated on the KLN–NTS lattice. The presence of Ni in the liquid phase indicates that Ni^{II} ions could act as new nucleus for the TTB crystallization. As higher the amounts of liquid phase, higher the TTB appearance.

Finally, the matrix grains (point 3, Fig. 5(b)) have the typical nominal composition with a Na/K concentration ratio around 1.12, slightly lower than the nominal ratio of 1.18 (see Fig. 5(e)). In addition, traces of Ni^{II} can be observed on these grains by EDS, but the solubility of NiO in the perovskite lattice is limited. The lattice cannot accommodate the nominal NiO content since it corresponds to B-site excess. Thus, the corresponding excess is directly compensated by the eviction of some Nb^{5+} ions, with transformation of the perovskite structure and formation of secondary phases, in accordance with the XRD results discussed above.

3.3. Dielectric properties

Fig. 6(a) shows the temperature dependence of the dielectric constant ε_r (at 100 kHz) of $(KNL)_{1-x}Ni_{x/2}$–NTS ceramics as function of x. Considering the evolution of the dielectric constant, two anomalies are observed: (i) a maximum at Curie temperature, T_c (~310 °C) corresponding to the tetragonal (ferroelectric)–cubic (paraelectric) phase transition and (ii) close to room temperature, a weak maximum, corresponding to the orthorhombic (ferroelectric)–tetragonal (ferroelectric) phase transition (O–T).

For the tetragonal-cubic transition, the value of ε_r at T_c decreases with the NiO content and reaches minimum value of ~3500 for $x = 0.05$. The T_c remains constant, while the temperature of the orthorhombic-tetragonal phase transition is increased by NiO addition, which corresponds well to the XRD observation. This evolution is different from the one generally observed for most of modified-KNN materials. Indeed, for these compounds, the substitutions in A and B-site generally decreases the phase transition temperatures: for example, the orthorhombic-tetragonal phase transition temperature is decreased by the Li^+ substitution in the A-site,[10,13,27] or by Sb^{5+} or Ta^{5+} substitution in B-site,[11,14] which stabilize the tetragonal phase at room temperature.[31] In the present case, the temperature at which this phase transition occurs is increased (see insert in Fig. 6(a)), which means that the modification mechanism is more complex. As for the structural distortion observed by XRD and Raman spectroscopy, no change is observed for low NiO contents, while the O–T phase transition temperature is increased for $x \geq 0.03$.

The phases transition for $(KNL)_{1-x}Ni_{x/2}$–NTS ceramics described here, could be explained by a simple pseudo phase diagram, as shown in Fig. 6(b). The pseudo phase diagram results indicate that the ferroelectric phase transition (T_c) remains constant with the NiO content. Nonetheless, the orthorhombic to tetragonal (T_{O-T}) phase transition is affected by the NiO addition, showing nearly constant value up to concentrations of $x = 0.01$, and experiencing an increase in transition temperature for higher Ni^{II} contents. This fact could indicate that Ni^{II} incorporation on the KNL–NTS structure occurs in two stages that would be discussed in Section 4.

Fig. 7(a) and (b) represent the room temperature dielectric properties of $(KNL)_{1-x}Ni_{x/2}$–NTS unpoled ceramics at different frequencies. The Ni^{II} addition globally induces a decrease of the relative permittivity (Fig. 7(c)), together with a slight increase

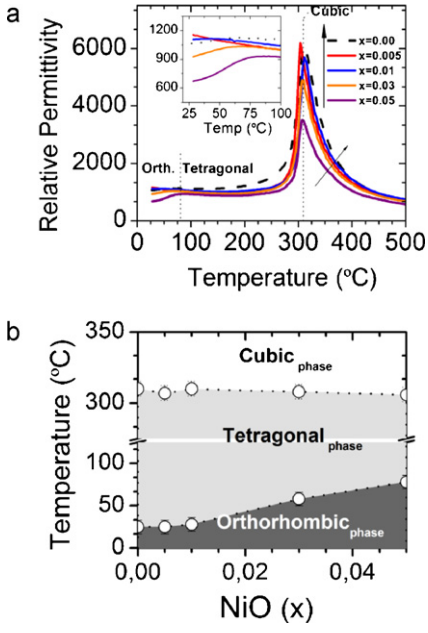

Fig. 6. (a) Temperature dependence of the relative permittivity for $(KNL)_{1-x}Ni_{x/2}$–NTS ceramics with different content of NiO. The part (b) shows the evolution of the T_c and the phase transition temperatures from orthorhombic to tetragonal phase (T_{O-T}) of the $(KNL)_{1-x}Ni_{x/2}$–NTS ceramics with different content in NiO (the sensitivity of the phase transition temperatures, T_{O-T} and T_c, were estimated on ±5 °C).

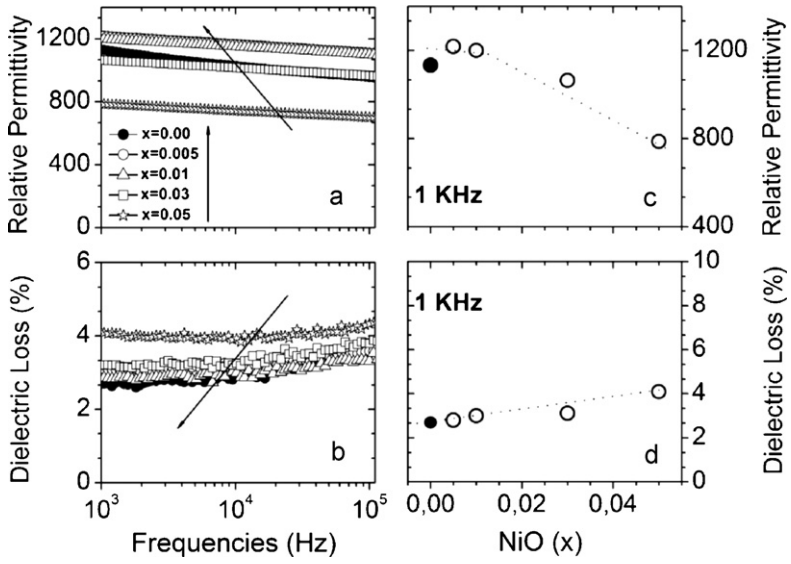

Fig. 7. (a) Relative permittivity and (b) dielectric losses as function of the frequency for $(KNL)_{1-x}Ni_{x/2}$–NTS ceramics with different NiO content. The part (c) shows the evolution of the dielectric constant at 1 kHz in the unpoled ceramics. The part (d) shows the evolution of the dielectric losses at 1 kHz in the unpoled ceramics.

of the dielectric losses (Fig. 7(d)), but all the ceramics present dielectric losses values lower than 4.1% at 1 kHz.

On the other hand, the dielectric constant for low NiO addition ($x \leq 0.01$) is higher than for the samples without NiO (Fig. 7(c)). Moreover, the relative permittivity response shows a large frequency-range with stability of the dielectric constant.

3.4. Piezoelectric properties

Fig. 8 represents the dependence of the piezoelectric properties (d_{ij}) and mechanical quality factor (Q_m) afforded by $(KNL)_{1-x}Ni_{x/2}$–NTS ceramics as a function of the NiO content. It can be observed how for low x values (≤ 0.01), the d_{33} and d_{31} values remains constant and the perovskite structure with tetragonal symmetry apparently remains unchanged. For higher Ni^{II} contents ($x \geq 0.03$), the d_{33} and d_{31} decrease gradually to ~115 pC/N and ~50 pC/N for the composition with the highest NiO content ($x = 0.05$).

A high Q_m value is desirable for resonant piezoelectric devices to suppress heat generation during the operation of the device.[32,33] In the literature, the Q_m values for undoped KNL–NTS are reported to be between 30[33] and 65.[34] When increasing NiO content, the Q_m factor was found to increase from 45 for samples without NiO to 145 for $x = 0.05$. Thus, the substitution of small amounts of cations modifies the dielectric and piezoelectric properties resulting in a reduction of the dielectric constant and of the piezoelectric activity, while the mechanical quality factor, Q_m, is increased.

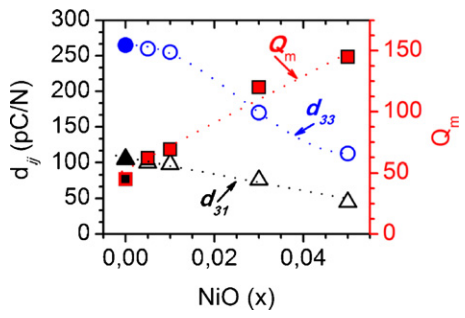

Fig. 8. Variations of the piezoelectric constants, d_{ij} and the planar mechanical quality, Q_m, with the amount of NiO in the $(KNL)_{1-x}Ni_{x/2}$–NTS ceramics. Standard tolerance: piezoelectric constant ± 5% (except for Q_m).

3.5. Ferroelectric properties

Fig. 9(a) shows room-temperature P–E hysteresis loops of the $(KNL)_{1-x}Ni_{x/2}$–NTS ceramics. Well-saturated hysteresis loops, with a good square shape, were clearly obtained in all samples. The remnant polarization, P_r, and coercive field, E_c, of undoped ceramics were previously found to be 18.2 μC/cm² and 15.8 kV/cm, respectively.[35] As for the structural evolution (XRD, Raman spectroscopy, phase transition temperatures, piezoelectric properties), two different ranges can be distinguished (Fig. 9(b)): when a small amount of NiO was added ($x \leq 0.01$), P_r remains constant while E_c is increased up to 20 kV/cm. For higher x values ($x > 0.01$), the P_r values grad-

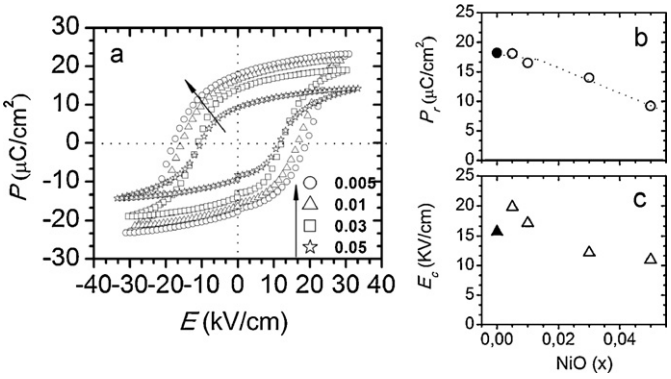

Fig. 9. (a) Polarization-field response of the for $(KNL)_{1-x}Ni_{x/2}$–NTS ceramics with different NiO content. Effect of Ni^{2+} addition on (b) remnant polarization, P_r, and (c) coercive field, E_c, of $(KNL)_{1-x}Ni_{x/2}$–NTS ceramics.

ually decreased from ~18.2 to 9.2 μC/cm^2 while E_c is also decreased to ~12 kV/cm. The decrease in P_r suggests that the addition of NiO weaken the ferroelectricity of the ceramics. Similar weakening effects have also been reported for other modified KNN-systems, such as KNN–CuO.[31]

4. Discussion

As it has been discussed above in Section 1, the ionic radius of Ni^{II} falls in the size range of A-site and B-site positions, and therefore Ni^{II} ion could potentially substitute in either A or B-site. Indeed, for transition metal elements, the most probable position is the B-site for crystal-chemistry considerations, but the incorporation of a limited content of Ni^{II} in A-site (~1%) cannot be excluded. In this work, we have shown that the evolution of the structural properties of the material present two different trends with the amount of Ni^{II} added. For low concentrations (below $x = 0.01$), lattice parameters remain nearly unchanged, whereas for higher concentrations an evident change for the lattice parameters take place, together with a change on the KNL–NTS crystal structure (see Figs. 2 and 6).

The following two equations using the Kröger–Vink's notation[36] describe the doping behavior of Ni^{II} in this system, respectively in A and B-sites of the perovskite lattice, for a global formula $A_2B_2O_6$:

$$(1-x)(A_2O)(B_2O_5) + x\mathrm{NiO} \rightarrow [A_{(1-x)}(Ni_A^{\bullet})_{x/2}(V'_A)_{x/2}]_2B_2O_6 \quad (2)$$

$$(A_2O)\left(1-\frac{x}{2}\right)(B_2O_5) + x\mathrm{NiO} \rightarrow A_2[B_{(2-x)}(Ni_B'''')_x]O_{6-3x/2}(V_o^{\bullet\bullet})_{3x/2} \quad (3)$$

The first mechanism corresponds to the creation of A-site vacancies (V'_A) while the second one is associated with the occurrence of oxygen vacancies ($V_o^{\bullet\bullet}$). The A-site vacancies generally facilitate the movement of the ferroelectric domain and made the polarization switching easier.[37] Oxygen vacancies are unfavorable to polarization switching, because they imply pinning of the domain walls and thus lead to an increase of coercive field (hardening effect) and also to a reduction in permittivity, dielectric and mechanical losses.

As noticed above, we selected a global formula, $(K_{0.44}Na_{0.52}Li_{0.04})_{(1-x)}Ni_{(x/2)}(Nb_{0.86}Ta_{0.10}Sb_{0.04})O_3$, which implies A-site deficiency, and would then mean the preferential incorporation on the A-site from compositional considerations, at least for low Ni^{II} concentrations. Then, when the amount of Ni^{II} is lower than $x = 0.01$, the Ni^{II} enters preferentially on the A-sites (donor-type doping), substituting K^+, Na^+ and Li^+ ions. Since the Ni^{II} radius is smaller than the ones of the A-site cations, no variations on the lattice parameters are expected by this substitution, but could cause a slack of the lattice and enhance the motion of 90° domains.[38] Coexistence of the motion of 90° and 180° domains leads to the stabilization of the piezoelectric properties.[35]

However, the solubility of Ni^{II} in the A-sites position of the perovskite is very limited. When the amount of Ni^{II} is over $x = 0.01$, Ni^{II} ions are supersaturated in the lattice of KNL–NTS, and the excess Ni^{II} ions enter on the B site of the lattice and favors the formation of the TTB secondary phase, as evidenced in Fig. 2(a) and (b). Moreover, the corresponding excess is directly compensated by the eviction of some Nb^{5+} ions, with formation of TTB secondary phase. As reported above, this one seems to correspond to $K_3LiNb_6O_{17}$ and thus includes some potassium and lithium. As the symmetry of the Li^+-substituted KNN materials is directly determined by the Li^+ content,[10,27] removing some lithium transforms the structure from orthorhombic to tetragonal, thus lowers the O–T phase transition temperature. The replacement of the (Nb/Ta/Sb) ions in B-site by larger Ni^{II} ions thus explains the reduction in the amplitude of the remnant polarization and in the piezoelectric properties,[39,40] together with the increase of Q_m.

This different tendency of $(KNL)_{1-x}Ni_{x/2}$–NTS system is reflected in the different trends observed for the structure, microstructure and particularly in the mechanical quality factor, Q_m.

5. Conclusions

The results have demonstrated how NiO can act as a dopant of KNL–NTS ceramics and their electric performance can be modulated through the addition of the appropriate Ni amounts. Considering our results, we can distinguish two different ranges doping levels. For low NiO contents, the structure remains tetragonal; the mechanical quality factor is slightly increased, while the piezoelectric coefficients d_{ij} and the remnant polarization remains quasi unmodified. The stabilization of the ferro-piezoelectric properties means that Ni^{II} could incorporate in A-site of the perovskite and thus acts as donor dopant.

For higher NiO contents, the B-excess introduced by our formula and the high amount of liquid phase induces the formation of a secondary phase, with tetragonal-tungsten bronze structure. This niobium-based secondary-phase removes some lithium from the A-site of the perovskite lattice and thus leads to an orthorhombic symmetry and an increase of the tetragonal-orthorhombic phase-transition temperature. Consequently all the properties are decreased (ε_r, d_{ij}, E_c, P_r), except for the mechanical quality factor which is increased.

Acknowledgments

The authors express their thanks to the MICINN (Spain) project MAT2010-21088-C03-01 for their financial support. Dr. F. Rubio-Marcos is also indebted to the "Conseil Regional du Limousin" for post-doctoral fellowship. Authors thank to C.A. Fernández-Godino for his assistance in the preparation of the compositions.

References

1. EU Directive 2002/95. http://ec.europa.eu/environment/waste/weee/index_en.htm.
2. Shrout TR, Zhang SJ. Lead-free piezoelectric ceramics: alternatives for PZT? *J Electroceram* 2007;**19**:113–26.
3. Matsubara M, Yamaguchi T, Sakamoto W, Kikuta K, Yogo T, Hirano S. Processing and piezoelectric properties of lead-free (K,Na)(NbTa)O_3 ceramics. *J Am Ceram Soc* 2005;**88**:1190–6.

4. Takao H, Saito Y, Aoki Y, Hiribuchi K. Microstructural evolution of crystalline-oriented $(K_{0.5}Na_{0.5})NbO_3$ piezoelectric ceramics with a sintering aid of CuO. *J Am Ceram Soc* 2006;**89**:1951–6.
5. Zuo R, Rödel J, Chen R, Li L. Sintering and electrical properties of lead-free $Na_{0.5}K_{0.5}NbO_3$ piezoelectric ceramics. *J Am Ceram Soc* 2006;**89**:2010–5.
6. Rubio-Marcos F, Navarro-Rojero MG, Romero JJ, Fernández JF. Effect of ZnO on the structure, microstructure and electrical properties of KNN-modified piezoceramics. *J Eur Ceram Soc* 2009;**29**:3045–52.
7. Bomlai P, Sinsap P, Muensit S, Milne SJ. Effect of MnO on the phase development, microstructures, and dielectric properties of $0.95Na_{0.5}K_{0.5}NbO_3$–$0.05LiTaO_3$ ceramics. *J Am Ceram Soc* 2008;**91**:624–7.
8. Kosec M, Kolar D. On activated sintering and electrical properties of $NaKNbO_3$. *Mater Res Bull* 1975;**10**:335–9.
9. Park HY, Ahn CW, Song HC, Lee JH, Nahm S, Uchino K, et al. Microstructure and piezoelectric properties of 0.95 $(Na_{0.5}K_{0.5})NbO_3$–$0.05BaTiO_3$ ceramics. *Appl Phys Lett* 2006;**89**:062906.
10. Guo Y, Kakimoto KI, Ohsato H. Phase transitional behavior and piezoelectric properties of $(Na_{0.5}K_{0.5})NbO_3$–$LiNbO_3$ ceramics. *Appl Phys Lett* 2004;**85**:4121.
11. López-Juárez R, González-García F, Zárate-Medina J, Escalona-González R, Díaz de la Torre S, Villafuerte-Castrejóna ME. Piezoelectric properties of Li–Ta co-doped potassium–sodium niobate ceramics prepared by spark plasma and conventional sintering. *J Alloys Compd* 2011;**509**:3837–42.
12. Skidmore TA, Milne SJ. Phase development during mixed-oxide processing of a $[Na_{0.5}K_{0.5}NbO_3]_{1-x}$–$[LiTaO_3]_x$ powder. *J Mater Res* 2007;**22**:2265–72.
13. Skidmore TA, Comyn TP, Milne SJ. Temperature stability of $([Na_{0.5}K_{0.5}NbO_3]_{0.93}$–$[LiTaO_3]_{0.07})$ lead-free piezoelectric ceramics. *Appl Phys Lett* 2009;**94**:222902.
14. Zang GZ, Wang JF, Chen HC, Su WB, Wang CM, Qi P, et al. Perovskite $(Na_{0.5}K_{0.5})_{1-x}(LiSb)_xNb_{1-x}O_3$ lead-free piezoceramics. *Appl Phys Lett* 2006;**88**:212908.
15. Saito Y, Takao H, Tani T, Nonoyama T, Takatori K, Homma T, et al. Lead-free piezoceramics. *Nature* 2004;**432**:84–7.
16. Ochoa DA, García JA, Pérez R, Gomis V, Albareda A, Rubio-Marcos F, et al. Extrinsic contributions and nonlinear response in lead-free KNN-modified piezoceramics. *J Phys D: Appl Phys* 2009;**42**:025402.
17. Shannon RD. Revised effective ionic radii and systematic studies of interatomie distances in halides and chaleogenides. *Acta Cryst* 1976;**A32**:751–67.
18. Rubio-Marcos F, Marchet P, Merle-Méjean T, Fernández JF. Role of sintering time, crystalline phases and symmetry in the piezoelectric properties of lead-free KNN-modified ceramics $(Li/Na/K)(Nb/Ta/Sb)O_3$. *Mater Chem Phys* 2010;**123**:91–7.
19. Rubio-Marcos F, Navarro-Rojero MG, Romero JJ, Marchet P, Fernández JF. Piezoceramics properties as a function of the structure in the system $(K,Na,Li)(Nb,Ta, Sb)O_3$. *IEEE Trans Ultrason Ferroelectr Freq Control* 2009;**56**:1835–42.
20. Wang Y, Damjanovic D, Klein N, Setter N. High-temperature instability of Li- and Ta-modified $(K,Na)NbO_3$ piezoceramics. *J Am Ceram Soc* 2008;**91**:1962–70.
21. Rubio-Marcos F, Ochoa P, Fernández JF. Sintering and properties of lead-free piezoceramics. *J Eur Ceram Soc* 2007;**27**:4125–9.
22. Rubio-Marcos F, Romero JJ, Fernández JF. Effect of the temperature on the synthesis of KNN-modified nanoparticles by a solid state reaction route. *J Nanopart Res* 2010;**12**:2495–502.
23. http://www.ferroperm-piezo.com.
24. Tanaka J, Onoda Y, Tsukioka M, Shimazu M, Ehara S, The RMN. Study of Li ion motion in $K_3LiNb_6O_{17}$ and K_3LiTaO_{17}. *Jpn J Appl Phys* 1982;**21**:451–5.
25. Lima KCV, Souza Filho AG, Ayala AP, Mendes Filho J, Freire PTC, Melo FEA, et al. Raman study of morphotropic phase boundary in $PbZr_{1-x}Ti_xO_3$ at low temperatures. *Phys Rev B* 2001;**63**:184105.
26. Lima JA, Paraguassu W, Freire PTC, Souza Filho AG, Paschoal CWA, Mendes Filho J, et al. Lattice dynamics and low-temperature Raman spectroscopy studies of PMN–PT relaxors. *J Raman Spectrosc* 2009;**40**:1144–9.
27. Klein N, Hollenstein E, Damjanovic D, Trodahl HJ, Setter N, Kuball M. A study of the phase diagram of $(K,Na, Li)NbO_3$ determined by dielectric and piezoelectric measurements, and Raman spectroscopy. *J Appl Phys* 2007;**102**:014112.
28. Kakimoto K, Akao K, Guo Y, Ohsato H. Raman scattering study of piezoelectric $(Na_{0.5}K_{0.5})NbO_3$–$LiNbO_3$ ceramics. *Jpn J Appl Phys* 2005;**44**:7064–7.
29. Hardcastle FD, Wachs I. Determination of niobium–oxygen bond distances and bond orders by Raman spectroscopy. *Solid State Ion* 1991;**45**:201–13.
30. Rubio-Marcos F, Bañares MA, Romero JJ, Fernández JF. Correlation between the piezoelectric properties and the structure of lead-free KNN-modified ceramics, studied by Raman spectroscopy. *J Raman Spectrosc* 2010;**42**:639–43.
31. Hollenstein E, Davis M, Damjanovic D, Setter N. Piezoelectric properties of Li- and Ta-modified $(K_{0.5}Na_{0.5})NbO_3$ ceramics. *Appl Phys Lett* 2005;**87**:182905.
32. Matsubara M, Yamaguchi T, Kikuta K, Hirano S. Sinterability and piezoelectric properties of $(K,Na)NbO_3$ ceramics with novel sintering aid. *Jpn J Appl Phys* 2004;**43**:7159–63.
33. Li E, Kakemato H, Wada S, Tsurumi T. Enhancement of Q_m by codoping of Li and Cu to potassium sodium niobate lead-free ceramics. *IEEE Trans Ultrason Ferroelectr Freq Control* 2008;**55**:980–7.
34. Marandian Hagh N, Kerman K, Jadidian B, Safari A. Dielectric and piezoelectric properties of Cu^{2+}-doped alkali niobates. *J Eur Ceram Soc* 2009;**29**:2325–32.
35. Rubio-Marcos F, Romero JJ, Ochoa DA, García JE, Perez R, Fernández JF. Effects of poling process on KNN-modified piezoceramic properties. *J Am Ceram Soc* 2010;**93**:318–21.
36. Kröeger FA. *Chemistry of imperfect crystals*. North-Holland, Amesterdam, Netherlands; 1964.
37. Ramana EV, Suryanarayana SV, Sankaram TB. Synthesis and magnetoelectric studies on $Na_{0.5}Bi_{0.5}TiO_3$–$BiFeO_3$ solid solution ceramics. *Solid State Sci* 2010;**12**:956–62.
38. Roy-Chowdhury P, Deshpande SB. Effect of dopants on the microstructure and lattice parameters of lead zirconate–titanate ceramics. *J Mater Sci* 1987;**22**:2209–15.
39. Zhong WL. *Physics of ferroelectrics*. Beijing, China: Science Press; 1996. p. 274–85.
40. Kamiya T, Suzuki T, Tsurumi T, Daimon M. Effects of manganese addition on piezoelectric properties of $Pb(Zr_{0.5}Ti_{0.5})O_3$. *Jpn J Appl Phys* 1992;**31**:3058–60.